Chemical Science

ROYAL SOCIETY OF CHEMISTRY

EDGE ARTICLE

View Article Online
View Journal | View Issue

Cite this: *Chem. Sci.*, 2023, **14**, 12637

All publication charges for this article have been paid for by the Royal Society of Chemistry

Received 5th September 2023
Accepted 12th October 2023

DOI: 10.1039/d3sc04682f

rsc.li/chemical-science

Template-assisted synthesis of isomeric copper(I) clusters with tunable structures showing photophysical and electrochemical properties†

Jun-Jie Fang, Zheng Liu, Yang-Lin Shen, Yun-Peng Xie * and Xing Lu *

A comparative study of structure–property relationships in isomeric and isostructural atomically precise clusters is an ideal approach to unravel their fundamental properties. Herein, seven high-nuclearity copper(I) alkynyl clusters utilizing template-assisted strategies were synthesized. Spherical Cu_{36} and Cu_{56} clusters are formed with a $[M@(V/PO_4)_6]$ (M: Cu^{2+}, Na^+, K^+) skeleton motif, while peanut-shaped Cu_{56} clusters feature four separate PO_4 templates. Experiments and theoretical calculations suggested that the photophysical properties of these clusters are dependent on both the inner templates and outer phosphonate ligands. Phenyl and 1-naphthyl phosphate-protected clusters exhibited enhanced emission features attributed to numerous well-arranged intermolecular C–H···π interactions between the ligands. Moreover, the electrocatalytic CO_2 reduction properties suggested that internal PO_4 templates and external naphthyl groups could promote an increase in C_2 products (C_2H_4 and C_2H_5OH). Our research provides new insight into the design and synthesis of multifunctional copper(I) clusters, and highlights the significance of atomic-level comparative studies of structure–property relationships.

Introduction

During the past few decades, atomically precise metal nanoclusters have contributed significantly to the rapid development of nanomaterials by elucidating structure–property relationships.[1–6] Alkynyl ligands have more abundant coordination modes than the commonly used thiolate and phosphine ligands, and therefore alkynyl-protected coinage metal clusters have remarkable structures.[7–11] However, the reaction between alkynyl ligands and Cu^+ often produces insoluble polymers, which increases the difficulty of synthesis and isolation.[12,13] To address this issue, template agents have been introduced into the synthesis process to balance the charge distribution of the clusters and prevent or interrupt the formation of insoluble polymers resulting from the reaction between alkynyl and Cu^+. As a result, the synthesis of high-nuclearity copper(I) alkynyl clusters with larger size and unique properties has been facilitated.[14–17]

Polyoxometalates (POMs) have attracted considerable attention due to their structural diversity and desirable properties in materials science, medicinal chemistry, and catalysis.[18–20] Previous studies have reported silver alkynyl clusters with richer structures and more unique properties constructed with POMs.[21–24] Polyoxovanadates and polyoxomolybdates, both members of the POM family, constitute a fascinating family of polynuclear oxo-anions that exhibit variable coordination geometries, but have a strong tendency to exhibit mixed-valent states,[25–27] which leads to the easy oxidation of Cu^+. This oxidizability significantly increases the difficulty in synthesizing copper(I) alkynyl clusters constructed with POMs.

Metal phosphonates not only exhibit various structures ranging from discrete molecules to multi-dimensional coordination polymers that provide a bridge for the construction of high-nuclearity metal clusters,[28–30] but also hold potential applications in biotechnology, water treatment, photochemistry, and magnetism.[31–34] We previously reported the use of $(^nBu/^tBu)PO_3H_2$ as precursors to construct a series of silver clusters. $(^nBu/^tBu)PO_3H_2$ units serve as tripod pillars that have a variety of coordination modes with metals and can be used as structure-directing templates to form enlarged composite clusters.[23,24,35–37] However, the reactions of polyoxometalates and phosphonates in this system are complicated, and V/P elements tend to exhibit multiple valent states that are prone to oxidize Cu^+. Consequently, it is more difficult to synthesize copper(I) clusters with POM or phosphonate templates than silver(I) clusters. So far, only a few successfully synthesized copper(I) alkynyl clusters constructed with POM or phosphonate templates have been reported, including Mak's previously reported Cu_{33},[38] Cu_{46},[39] Cu_{47},[39] Cu_{62} (ref. [38]) and our reported Cu_{25}.[40]

State Key Laboratory of Materials Processing and Die & Mould Technology, School of Materials Science and Engineering, Huazhong University of Science and Technology, Wuhan 430074, China. E-mail: xieyp@hust.edu.cn; lux@hust.edu.cn

† Electronic supplementary information (ESI) available. CCDC 2219441, 2116536, 2285409, 2219449, 2219459, 2219463, 2219464 and 2219447. For ESI and crystallographic data in CIF or other electronic format see DOI: https://doi.org/10.1039/d3sc04682f

Recently, atomically precise copper clusters and their correlations between structures and properties have received a lot of attention, particularly with regard to photoluminescence[41,42] and CO_2 reduction reaction (CO_2RR).[43–45] For example, Jin *et al.* found that the phosphorescence quantum efficiency of M@Cu_{14} (M: Au, Cl) nanoclusters can be tuned by a single-atom kernel.[46] Zang *et al.* observed that Au doping in the innermost shell of $Au_{12}(AgCu)_{38}$ significantly enhances near-infrared photoluminescence intensity.[47] Bakr *et al.* reported that extended C–H···π and π···π intermolecular ligand interactions significantly enhance photoluminescence.[48] Atomically precise clusters with well-defined architectures and chemical compositions have attracted attention in the field of heterogeneous catalysis.[49–53] For instance, Liu *et al.* synthesized $Cu_{32}H_{20}L_{12}$ (L: $S_2P(O^iPr)_2$) exhibiting high selectivity (FE_{HCOOH} = 89% at −0.3 V, 83% at −0.4 V) for the CO_2RR.[54] Zang *et al.* observed that ditetrahedron-shaped Cu_8 exhibited a higher FE_{HCOOH} (≈92%) at −1.0 V than the cube-shaped Cu_8.[55] Tang *et al.* reported that M_{15} (Au_7Ag_8, Ag_9Cu_6, and $Au_2Ag_8Cu_5$) exhibits drastically different CO_2RR performances in a wide voltage range.[56] These atomically precise clusters facilitate systematic comparative studies of structure–property relationships.

In this study, we designed a synthesis strategy to address the aforementioned challenges by adding weak reducing agents and phosphonate ligands, successfully synthesizing seven copper(I) alkynyl clusters. Single crystal structure analysis revealed that the structural modulation of these clusters can be achieved through the bonding of metal cations to templates. One Cu^{2+}, Na^+, or K^+ ion captured by six VO_4 or PO_4 tetrahedrons constructs a [M@(V/PO_4)$_6$] (M: Cu^{2+}, Na^+, K^+) skeleton, which tends to form structurally similar spherical Cu_{36} and Cu_{56} clusters. Meanwhile, in the reaction system where Na^+ and K^+ ions are replaced with NH_4^+, peanut-shaped Cu_{56} clusters can be constructed from four PO_4 tetrahedrons. The crystalline-state emissions of these clusters depend on the inner templates and the outer phosphonate ligands. The surfaces of $PhOPO_3^{2-}$ and 1-$NaphOPO_3^{2-}$ protected clusters are interconnected through numerous well-arranged intermolecular C–H···π interactions between the ligands of adjacent clusters, leading to enhanced emission. Electrocatalytic measurements of CO_2 reduction reaction showed that PO_4-encapsulated Cu_{56} possesses higher catalytic activity for the CO_2RR than VO_4-encapsulated Cu_{56}, and the PO_4 template and external naphthyl group can improve the yield of C_2 products (C_2H_4 and C_2H_5OH).

Results and discussion

Synthesis and general characterization

The synthesis of clusters, $[Cu^{II}(VO_4)_6@Cu^{I}_{36}(^tBuPO_3)_6(V_3O_3OH)(V_3O_6OH)(^tBuC{\equiv}C)_{18}]$ (**1**), $[Cu^{II}(VO_4)_6@Cu^{I}_{56}(^tBuPO_3)_6(^tBuC{\equiv}C)_{26}]F_2$ (**2**), $[Na^{I}(PO_4)_6@Cu^{I}_{56}(^tBuPO_3)_6(^tBuC{\equiv}C)_{26}]F$ (**3-Na**), $[K^{I}(PO_4)_6@Cu^{I}_{56}(^tBuPO_3)_6(^tBuC{\equiv}C)_{26}]F$ (**3-K**), $[Na^{I}(PO_4)_6@Cu^{I}_{56}(PhOPO_3)_6(^tBuC{\equiv}C)_{26}]F$ (**3-PhOPO$_3$**, $PhOPO_3$ = phenyl phosphate), $[Na^{I}(PO_4)_6@Cu^{I}_{56}$(1-$NaphOPO_3$)$_6$(-$^tBuC{\equiv}C)_{26}]F$ (**3-NaphOPO$_3$**, 1-$NaphOPO_3$ = 1-naphthyl phosphate), $[(PO_4)_4@Cu^{I}_{56}$(1-$NaphOPO_3$)$_6$($^tBuC{\equiv}C)_{32}]$ (**4**), requires meticulous control over various phosphonates and vanadates.

To achieve this, we employed three different phosphonate ligands with varying steric hindrances to regulate their structures (Fig. 1). Reaction conditions were optimized to obtain the crystalline products, including the ratio of template precursors and (^{t}Bu/PhO/1-NaphO)PO_3H_2 ligands, time of ultrasonic conditions, amount of Et_3N used, amount of $PhMe_2SiH$ added, and solvothermal temperature. Adjusting the addition ratio of NH_4VO_3 and $^tBuPO_3H_2$ allowed us to obtain single crystals of **1** and **2**. It should be noted that precise control of the amount of $PhMe_2SiH$ added was crucial to overcome the oxidizability of template precursors. Under natural light, the appearance of single crystals of **1–4** is dark red blocky and yellow blocky, respectively (Fig. S1†).

We elucidated the molecular structures of **1–4** through single crystal X-ray diffraction (SCXRD), and we have listed their crystal data, structure refinement, and selected bond lengths in ESI Tables 1, 2 and 5–12.† SCXRD analysis revealed that clusters **1** and **4** are both neutral clusters. While crystals of **1** and **4** are insoluble in common solvents, other crystals dissolve easily in CH_2Cl_2, CH_3OH, and CH_3CH_2OH, providing opportunities to examine their solution stabilities and ionic valences using electrospray ionization mass spectrometry (ESI-MS). For example, in the positive ion mode ESI-MS of **2** dissolved in CH_3OH and CH_2Cl_2, the two-charge prominent peaks centered at m/z = 3598.27 (**2-a**), 3608.24 (**2-b**), and 3617.23 (**2-c**) are assigned formulas of $[Cu^{II}@(VO_4)_6@Cu^{I}_{56}(^tBuPO_3)_6(^tBuC{\equiv}C)_{25}F_2 + H^+]^{2+}$ (calcd m/z = 3598.54), $[Cu^{II}@(VO_4)_6@Cu^{I}_{56}(^tBuPO_3)_6(^tBuC{\equiv}C)_{25}F_2 + H_2O + H^+]^{2+}$ (calcd m/z = 3608.05), and $[Cu^{II}@(VO_4)_6@Cu^{I}_{56}(^tBuPO_3)_6(^tBuC{\equiv}C)_{25}F_2 + (H_2O)_2 + H^+]^{2+}$ (calcd m/z = 3617.05), respectively (Fig. 2). We accurately identified other species produced by ionization of one or two $^tBuC{\equiv}C^-$ ligands from the cations of the pristine clusters or by

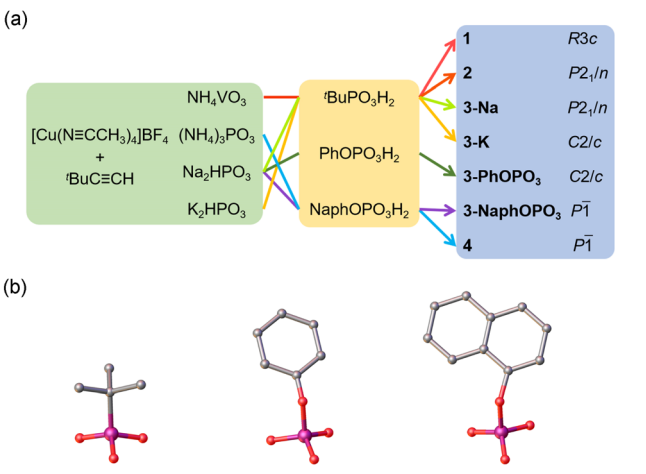

Fig. 1 Synthetic route and structures of phosphonate ligands. (a) Synthetic route for **1–4**. (b) Molecular structures of $^tBuPO_3H_2$, $PhOPO_3H_2$, and 1-$NaphOPO_3H_2$ ligands. Color codes: P, purple; O, red; C, gray. Hydrogen atoms are omitted for clarity.

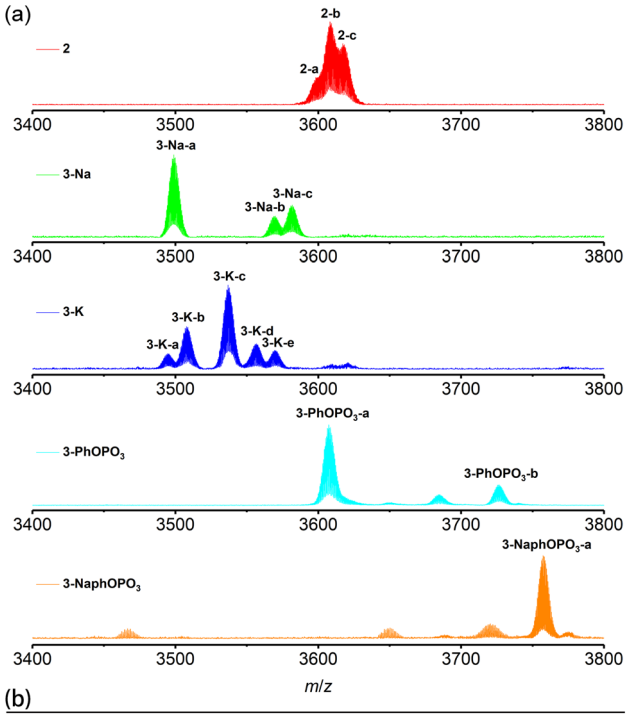

(b)

Species	Formula	Calcd. *m/z*	Exp. *m/z*
2-a	$[Cu^{I}@(VO_4)_6@Cu^{I}_{56}(^{t}BuPO_3)_6(^{t}BuC{\equiv}C)_{25}F_2{+}H^{+}]^{2+}$	3598.54	3598.27
2-b	$[Cu^{I}@(VO_4)_6@Cu^{I}_{56}(^{t}BuPO_3)_6(^{t}BuC{\equiv}C)_{23}F_2{+}H_2O{+}H^{+}]^{2+}$	3608.05	3608.24
2-c	$[Cu^{I}@(VO_4)_6@Cu^{I}_{56}(^{t}BuPO_3)_6(^{t}BuC{\equiv}C)_{23}F_2{+}(H_2O)_2{+}H^{+}]^{2+}$	3617.05	3617.23
3-Na-a	$[Na^{I}@(PO_4)_6@Cu^{I}_{56}(^{t}BuPO_3)_6(^{t}BuC{\equiv}C)_{25}]^{2+}$	3499.14	3498.91
3-Na-b	$[Na^{I}@(PO_4)_6@Cu^{I}_{56}(^{t}BuPO_3)_6(^{t}BuC{\equiv}C)_{26}F{+}H_2O{+}H^{+}{+}Na^{+}]^{2+}$	3570.18	3569.93
3-Na-c	$[Na^{I}@(PO_4)_6@Cu^{I}_{56}(^{t}BuPO_3)_6(^{t}BuC{\equiv}C)_{25}F{+}Cu^{I}F{+}Cu^{+}]^{2+}$	3582.08	3581.80
3-K-a	$[K^{I}@(PO_4)_6@Cu^{I}_{56}(^{t}BuPO_3)_6(^{t}BuC{\equiv}C)_{24}F{+}(H_2O)_2]^{2+}$	3494.11	3494.71
3-K-b	$[K^{I}@(PO_4)_6@Cu^{I}_{56}(^{t}BuPO_3)_6(^{t}BuC{\equiv}C)_{25}]^{2+}$	3507.13	3507.83
3-K-c	$[K^{I}@(PO_4)_6@Cu^{I}_{56}(^{t}BuPO_3)_6(^{t}BuC{\equiv}C)_{25}F{+}H_2O{+}Na^{+}]^{2+}$	3537.12	3536.87
3-K-d	$[K^{I}@(PO_4)_6@Cu^{I}_{56}(^{t}BuPO_3)_6(^{t}BuC{\equiv}C)_{26}{+}H_2O{+}H^{+}]^{2+}$	3557.17	3556.83
3-K-e	$[K^{I}@(PO_4)_6@Cu^{I}_{56}(^{t}BuPO_3)_6(^{t}BuC{\equiv}C)_{26}F{+}H^{+}{+}Na^{+}]^{2+}$	3569.16	3569.33
3-PhOPO$_3$-a	$[Na^{I}@(PO_4)_6@Cu^{I}_{56}(PhOPO_3)_6(^{t}BuC{\equiv}C)_{25}]^{2+}$	3607.03	3607.41
3-PhOPO$_3$-b	$[Na^{I}@(PO_4)_6@Cu^{I}_{56}(PhOPO_3)_6(^{t}BuC{\equiv}C)_{26}F{+}Cu^{I}F{+}CH_3OH{+}Na^{+}{+}H^{+}]^{2+}$	3727.04	3726.65
3-NaphOPO$_3$-a	$[Na^{I}@(PO_4)_6@Cu^{I}_{56}(NaphOPO_3)_6(^{t}BuC{\equiv}C)_{25}]^{2+}$	3757.08	3757.29

Fig. 2 Electrospray ionization mass spectra. (a) Experimental isotope distributions of selected peaks for **2–3-NaphOPO$_3$** (positive-ion mode, dissolved in CH_2Cl_2 and CH_3OH mixed solution). (b) The table is the formula assignment for these peaks.

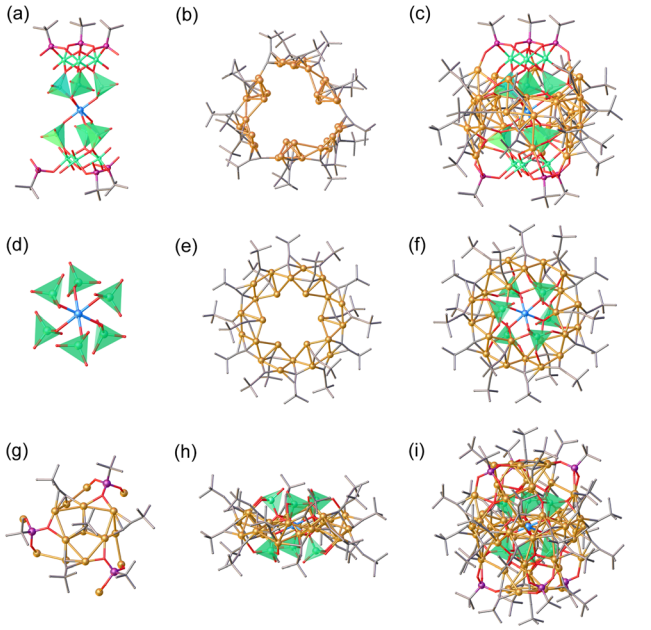

Fig. 3 The detailed structure analysis of **1** and **2**. VO_4 tetrahedrons are highlighted in green. (a) $[Cu^{II}(VO_4)_6@(^{t}BuPO_3)_6(V_3O_3OH)(V_3O_6OH)]^{18-}$ skeleton. (b) $[Cu_{36}(^{t}BuC{\equiv}C)_{18}]^{18+}$ ring. (c) Overview of the total structure of $[Cu^{II}(VO_4)_6@Cu^{I}_{36}(^{t}BuPO_3)_6(V_3O_3OH)(V_3O_6OH)(^{t}BuC{\equiv}C)_{18}]$. (d) $[Cu^{II}@(VO_4)_6]^{16-}$ kernel. (e) Wreath-shaped $[Cu_{24}(^{t}BuC{\equiv}C)_{18}]^{6+}$ ring. (f) Wheel-shaped $[Cu^{II}@(VO_4)_6@Cu_{24}(^{t}BuC{\equiv}C)_{18}]^{10-}$ unit viewed from the *c*-axis. (g) Cap-shaped $[Cu_{16}(^{t}BuC{\equiv}C)_4(^{t}BuPO_3)_3]^{6+}$ peripheral structural unit. (h) Wheel-shaped $[Cu^{II}@(VO_4)_6@Cu_{24}(^{t}BuC{\equiv}C)_{18}]^{10-}$ unit viewed from the *b*-axis. (i) Overview of the total structure of $[Cu^{II}@(VO_4)_6@Cu^{I}_{56}(^{t}BuPO_3)_6(^{t}BuC{\equiv}C)_{26}]^{2+}$. Color codes: Cu^{I}, yellow; Cu^{II}, light blue; V, green; P, purple; O, red; C, gray. Hydrogen atoms are omitted for clarity.

further addition of H^+, Na^+, or H_2O, indicating that these clusters are well stabilized in solution (Fig. S10–S15†).

Powder X-ray diffraction (PXRD) patterns of them *versus* the calculated patterns from single-crystal X-ray diffraction revealed their high phase purity, as shown in Fig. S16.† Their good thermal stability under the crystalline-state below 220 °C is exhibited in their thermogravimetric analysis (TGA) diagrams (Fig. S17†). Taking sample **2** as an example, the major weight loss (56.9%) in the range of 300–440 °C corresponds to a large proportion of ligand ($^{t}BuC{\equiv}C^-$ and $^{t}BuPO_3{}^{2-}$) decomposition, with a second weight loss (1.5%) between 440 and 800 °C that may be attributed to a fraction of ligand ($^{t}BuC{\equiv}C^-$ and $^{t}BuPO_3{}^{2-}$), Cu^{I}, and $[VO_4]^{3-}$ volatilization. The Fourier transform infrared (FT-IR) spectra confirmed the existence of alkynyl (2090 cm^{-1}) in these clusters (Fig. S18†).

Crystal structures of 1–4

Metal clusters can be synthesized using a variety of building blocks, and as previously reported, cap-shaped $[VO_2(OH)(^{t}BuPO_3)]^{2-}$, $[(VO_2)(^{t}BuPO_3)_2]^{3-}$, $[V_3O_6(OH)(^{t}BuPO_3)_3]^{4-}$, and $[V_4O_8(^{t}BuPO_3)_4]^{4-}$ units have been found to be versatile for the anion-templated synthesis of high-nuclearity silver(I) clusters.[24,37] Herein we report the successful formation of copper clusters using $[VO_4]^{3-}$/$[PO_4]^{3-}$ tetrahedrons and $[(^{t}Bu/PhO/1\text{-}NaphO)PO_3]^{2-}$ ligands as demonstrated in Fig. 3. The resulting cluster **1** crystallizes in the *R3c* space group, being assembled from one penetrating $[Cu^{II}(VO_4)_6@(^{t}BuPO_3)_6(V_3O_3OH)(V_3O_6OH)]^{18-}$ skeleton and one $[Cu^{I}_{36}(^{t}BuC{\equiv}C)_{18}]^{18+}$ ring at the waist with argentophilic Cu···Cu bond distances in the range 2.511–3.016 Å. The $[Cu^{I}_{36}(^{t}BuC{\equiv}C)_{18}]^{18+}$ ring has a van der Waals diameter of approximately 19.8 Å (Fig. S2†). The oxidizability of vanadate *in situ* generated a Cu^{2+} cation,[39] which is bridged by six $[VO_4]^{3-}$ tetrahedrons, forming an elongated octahedral coordination geometry $Cu^{II}O_6$.

By reducing the addition of vanadates and reaction time, cluster **2** was successfully synthesized. Furthermore, clusters **3-Na**, **3-K**, **3-PhOPO$_3$**, and **3-NaphOPO$_3$** were obtained by replacing vanadates with phosphonates resulting in crystal structures similar to cluster **2**. For instance, SCXRD analysis and ESI-MS revealed that the overall charge balance of cluster **2** against the cationic cluster is provided by two F^- counteranions. As

shown in Fig. 3, spherical cluster **2** has a multishelled core architecture of $Cu^{II}@(VO_4)_6@Cu^{I}_{56}(^tBuPO_3)_6(^tBuC{\equiv}C)_{26}$, with argentophilic Cu···Cu bond distances in the range 2.423–3.055 Å. Furthermore, the *in situ* generated Cu^{2+} cation is encapsulated in six $[VO_4]^{3-}$ templates. The wreath-shaped $[Cu_{24}(^tBuC{\equiv}C)_{18}]^{6+}$ ring has a hexagonal inner Cu_{12} unit, which is connected with the $[Cu^{II}@(VO_4)_6]^{16-}$ polyoxoanion template to form the wheel-shaped $[Cu^{II}@(VO_4)_6@Cu_{24}(^tBuC{\equiv}C)_{18}]^{10-}$ unit with a van der Waals diameter of about 20.4 Å (Fig. S2†). Cluster **2** is formed by fusing two cap-like $[Cu_{16}(^tBuC{\equiv}C)_4(^tBuPO_3)_3]^{6+}$ peripheral structural units staggered exactly by 60° on the upper and lower sides of the wheel-shaped unit. The packing pattern of crystal **2** shows that these molecules are well-arranged through intermolecular C–H···F interactions (4.079, 4.119, and 4.244 Å) (Fig. S3†).

Both spherical copper clusters, Cu_{36} and Cu_{56}, have similar internal distorted octahedron kernels, which are often observed in POMs.[57] As shown in Fig. 4, internal elongated MO_6 octahedron skeletons are regulated by external distinct cap-shaped units. Specifically, the $Cu^{II}O_6$ octahedron of cluster **1** has $Cu^{II}\cdots O_V$ (O_V: oxygen atom of the $[VO_4]^{3-}$ templates) bond distances ranging between 2.071 and 2.083 Å, whereas the $Cu^{II}\cdots O_V$ bond distances in cluster **2**, capped by $[Cu_{16}(^tBuC{\equiv}C)_4(^tBuPO_3)_3]$ units, are longer and range between 2.265, 2.270 and 2.310 Å. Additionally, cluster **3-K** has a K^+ ion core with a larger ion radius than the Na^+ ion, causing a larger KO_6 octahedron ($K\cdots O_P$ (O_P: oxygen atom of the $[PO_4]^{3-}$ templates) bond distances: 2.634, 2.635, and 2.669 Å) than the NaO_6 octagonal. The steric hindrances of outer phosphonate ligands increase from $^tBuPO_3^{2-}$, $PhOPO_3^{2-}$ to $1\text{-}NaphOPO_3^{2-}$, resulting in a gradual increase of the internal NaO_6 octagon size and the change of the space group from $P2_1/n$, $C2/c$, to $P\bar{1}$.

In the reaction system where Na_2HPO_3 and K_2HPO_3 are replaced by $(NH_4)_3PO_3$, cluster **4** can be constructed from PO_4 tetrahedrons without the presence of Na^+ or K^+ ions. As shown in Fig. 5, cluster **4** possesses a peanut-shaped structure that consists of four separate $[PO_4]^{3-}$ tetrahedrons, thirty-two $^tBuC{\equiv}C^-$ ligands, six $1\text{-}NaphOPO_3^{2-}$ ligands, and fifty-six Cu^+ ions with argentophilic Cu···Cu bond distances ranging from 2.401 to 3.056 Å. The absence of metal cations inside the cluster allows for the aggregation of $[PO_4]^{3-}$ tetrahedrons into the cluster. Cluster substructures $[(PO_4)_2@Cu^{I}_{28}(1\text{-}NaphOPO_3)(^tBuC{\equiv}C)_{16}]^{4+}$ are bridged by four $1\text{-}NaphOPO_3^{2-}$ ligands, with each oxygen atom coordinated to one copper atom.

It is noteworthy that the replacement of $^tBuPO_3^{2-}$ ligands with $PhOPO_3^{2-}$ and $1\text{-}NaphOPO_3^{2-}$ ligands leads to the

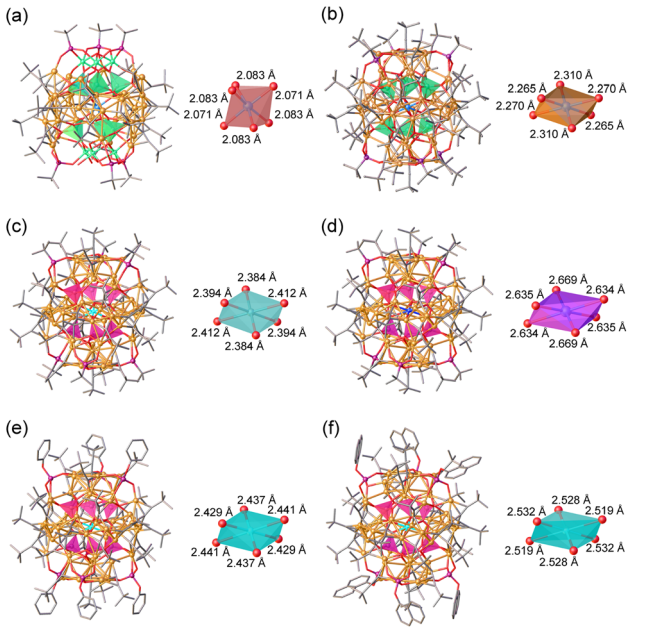

Fig. 4 Overview of the total structures of spherical Cu_{36} and Cu_{56} clusters, and their internal distorted MO_6 (M: Cu^{2+}, Na^+, K^+) octahedron kernels. (a) **1**, (b) **2**, (c) **3-Na**, (d) **3-K**, (e) **3-PhOPO$_3$**, and (f) **3-NaphOPO$_3$**. Color codes: Na, light blue; K, dark blue; Cu^I, yellow; Cu^{II}, sky blue; V, green; P, purple; O, red; C, gray. Hydrogen atoms are omitted for clarity.

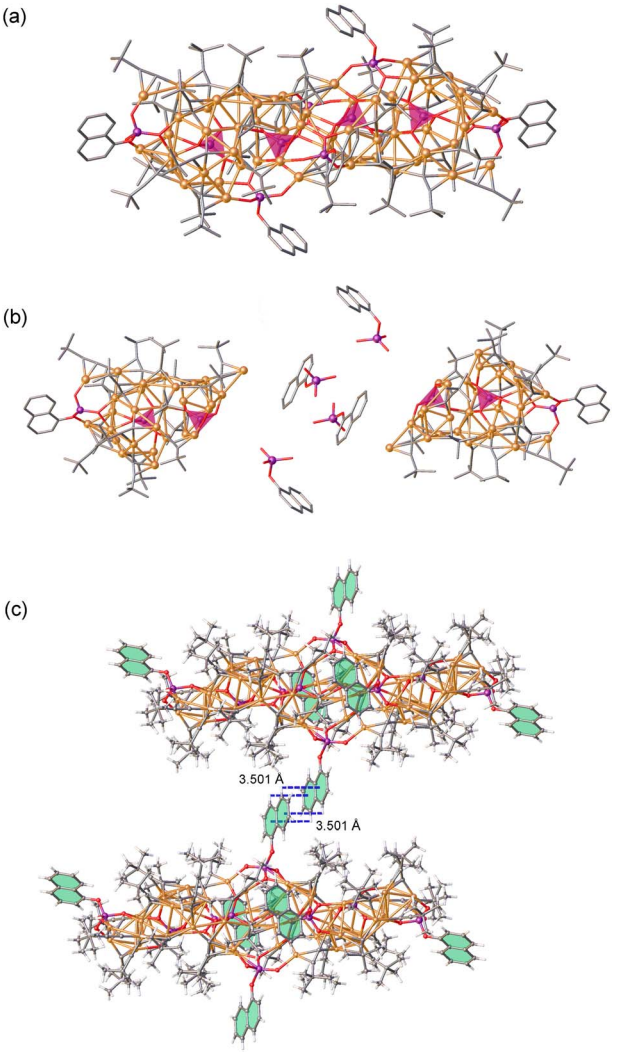

Fig. 5 The detailed structure analysis of **4**. PO_4 tetrahedrons are highlighted in pink. (a) Peanut-shaped $[(PO_4)_4@Cu^{I}_{56}(1\text{-}NaphOPO_3)_6(^tBuC{\equiv}C)_{32}]$. (b) Two asymmetric units of **4** bridged by four $1\text{-}NaphOPO_3^{2-}$ ligands. (c) The intermolecular C–H···π interactions between $1\text{-}NaphOPO_3^{2-}$ ligands of adjacent clusters in **4**. Color codes: Cu, yellow; P, purple; C, gray; O, red; H, white.

formation of numerous strong intermolecular C–H···π interactions between adjacent clusters. Fig. S6–S8† demonstrate how nearby 1-NaphOPO$_3^{2-}$ and ^{t}BuC≡C$^-$ ligands in cluster **4** form intermolecular C–H···π interactions at distances ranging from 2.862 to 3.626 Å. In cluster **3-PhOPO$_3$**, intermolecular C–H···π interactions (at distances of 3.479 and 3.754 Å) are formed by PhOPO$_3^{2-}$ ligands, while in cluster **3-NaphOPO$_3$**, intermolecular C–H···π interactions (at distances of 2.821, 3.342, and 3.598 Å) are formed by 1-NaphOPO$_3^{2-}$ ligands. These strong interactions between adjacent clusters are crucial to their luminous properties.

The coordination modes of alkynyl and phosphonate ligands with Cu$^+$ result in a diverse range of crystal structures, as demonstrated in Fig. S9.† Seven coordination modes, including μ_2-η_σ^1, η_π^1; μ_3-η_σ^1, η_σ^1, η_π^1; μ_3-η_σ^1, η_π^1, η_π^1.; μ_3-η_σ^1, η_σ^1, η_σ^1; μ_4-η_σ^1, η_σ^1, η_σ^1, η_σ^1; μ_4-η_σ^1, η_σ^1, η_σ^1, η_π^1; μ_4-η_σ^1, η_σ^1, η_π^1, η_π^1, are observed. Overall, the introduction of multiple VO_4 and PO_4 tetrahedrons with abundant terminal oxygen atoms during the synthesis of copper(I) alkynyl clusters not only balances the positive charges on the Cu(I) shells, but also effectively prevents or interrupts insoluble polymers formed by the reaction of alkynyl with Cu$^+$.

Photophysical properties

The optical properties of seven Cu_{36} and Cu_{56} clusters in their crystalline state were investigated through a series of spectroscopic analyses (Fig. 6a). The absorption features of clusters constructed by VO_4 tetrahedrons were found to be similar. Similarly, the absorption features of clusters constructed by PO_4 tetrahedrons had peaks located at 200–400 and 720 nm (except **4**), indicating that the electronic structures of these clusters are similar and in agreement with the single crystal data. The analysis of the absorption spectra revealed that clusters constructed by PO_4 tetrahedrons have an optical band gap in the range of 1.93–2.64 eV (Fig. S19†).

Photoluminescence (PL) properties correlate with both the optical absorption behaviors and crystal structures.[58,59] The PL spectra of cluster **2** in its crystalline state showed emission peaks at 444, 468, 507, 572, 654, and 670 nm, indicating a mechanism of multiple-exciton emission (Fig. 6b). As the temperature decreased, the luminescence intensity increased slightly, while the peak position remained unchanged. No luminescence thermochromism was observed, indicating that temperature has little effect on the tight packing and bond lengths in the crystal structure (argentophilic Cu···Cu bond average distances of 2.723 Å and 2.710 Å were observed in **2** and **2-100 K**, respectively). Clusters **1** and **4** both exhibited yellow emission centered at 574 nm. Meanwhile, **2-Na**, **2-K**, **3-PhOPO$_3$**, and **3-NaphOPO$_3$** exhibited a main emission peak at 430 nm and a shoulder peak at 710 nm.

The photoluminescence quantum yield (PLQY) of these clusters ranges from 1.05% to 3.65% (ESI Table 3†). Clusters protected by PhOPO$_3^{2-}$ and 1-NaphOPO$_3^{2-}$ ligands exhibited three times higher luminescence intensity than those protected by ^{t}BuPO$_3^{2-}$ ligands. There was a slightly enhanced quantum yield for clusters protected by PhOPO$_3^{2-}$ and 1-NaphOPO$_3^{2-}$ ligands. The strong intramolecular C–H···π interactions

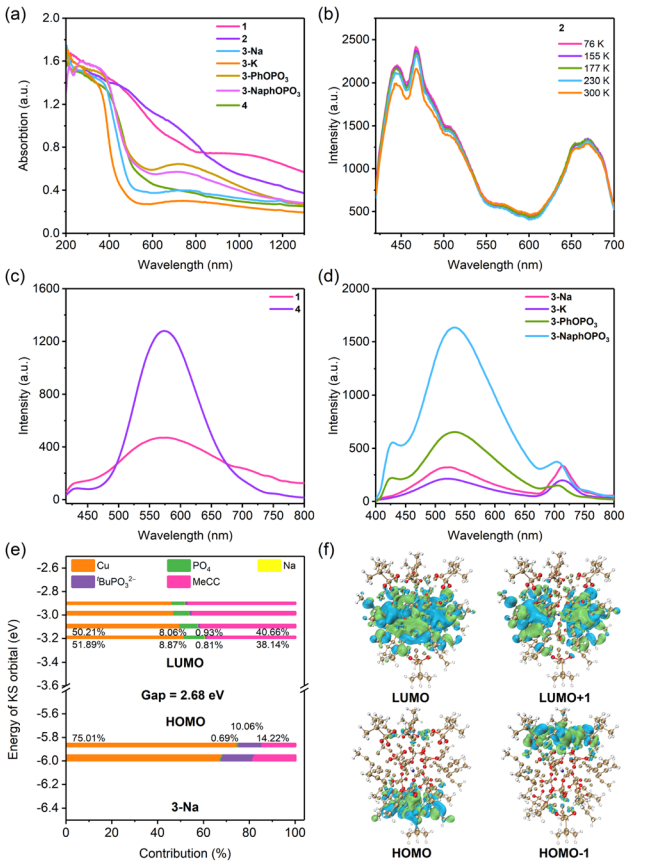

Fig. 6 Optical properties and electronic structures of clusters Cu_{36} and Cu_{56} in the crystalline state (λ_{ex} = 380 nm). (a) UV-Vis absorption spectra. (b) Temperature-dependent emission spectra of **2**. (c) Photoluminescence emission spectra of **1** and **4**. (d) Photoluminescence emission spectra of **3-Na**, **3-K**, **3-PhOPO$_3$**, and **3-NaphOPO$_3$**. (e) Composition analysis of frontier Kohn–Sham orbitals of **3-Na**. (f) Electronic density diagrams of the HOMO−1, HOMO, LUMO, and LUMO+1 of **3-Na** (isovalue = 0.010 a.u.).

connecting adjacent clusters restrict the rotation and vibration of some ^{t}BuC≡C$^-$, PhOPO$_3^{2-}$, and 1-NaphOPO$_3^{2-}$ ligands and effectively decrease nonradiative decay, accounting for the enhanced emission. The PL lifetime decay curves of each metal cluster were examined to determine the key characteristics of their excited state dynamics. For **2**, decay curves of the 468 and 670 nm peaks were well fitted using a double exponential function, while other clusters required a triple exponential function for adequate fitting (Fig. S20–S22 and Table S3†). The exciton lifetimes τ_1 and τ_2 for the 670 nm peak of **2** at 300 K were determined to be 4.36 (97.72%) and 59.23 ns (2.28%), respectively, and were observed to remain relatively stable at different temperatures. In contrast, other clusters were found to have a contribution from microsecond lifetime processes; for example, in **3-Na**, the exciton lifetimes τ_1, τ_2, and τ_3 for the 670 nm peak were determined to be 38.20 (62.79%), 361.17 (21.31%), and 2315.16 ns (15.90%), respectively.

To further elucidate the PL mechanism, density functional theory (DFT) calculations were performed using the ORCA 5.0.3 program.[60,61] Based on the single-crystal data, ^{t}BuC≡C$^-$ was

replaced with MeC≡C$^-$ to reduce the computational cost. In Fig. 6 and S23–S26,† the highest occupied molecular orbitals (HOMO and HOMO−1) of spherical Cu_{56} clusters were mainly located on the upper and lower cap-shaped structural units, while the lowest unoccupied molecular orbitals (LUMO and LUMO+1) were distributed on the wheel-shaped structural units at the waist. Comparative analysis of the contribution of different components to the LUMO and HOMO suggests that the PL mechanism arises from alkynyl → Cu(I) ^{3}LMCT (ligand to metal charge transfer) excited states that are modified by encapsulated templates and outer phosphonate ligands within the crystal structure.[62]

Electrochemical properties

ESI-MS reveals that ^{t}BuC≡C$^-$ ligands can be isolated from the as-prepared clusters in solution. Fig. S27† illustrates the space-filling model structures of the spherical Cu_{56} clusters with the removal of a ^{t}BuC≡C$^-$ ligand exposing several active sites formed by the Cu atoms. These spherical Cu_{56} clusters have similar configurations while differing in terms of their encapsulated templates and external phosphonate ligands, which could result in distinct catalytic behaviors for the CO_2RR.[55]

We conducted electrochemical experiments on **2**, **3-Na**, and **3-NaphOPO$_3$** clusters for the CO_2RR at different constant current densities (−50 to −500 mA cm^{-2}) in a flow cell, analyzing the gas and liquid products by gas chromatography (GC) and ^{1}H NMR, respectively. At low current densities HCOOH, CO, and H_2 are the primary products, while at higher current densities, C_2H_4 and C_2H_5OH emerge in greater quantities (Fig. 7 and S28–S32†). Among these clusters, **3-Na** and **3-NaphOPO$_3$** display similar CO_2RR properties. As the applied current density increases (−50 to −500 mA cm^{-2}), the faradaic efficiency for C_1 products initially rises and subsequently declines gradually, whereas the faradaic efficiency for C_2 products ($FE_{C_2H_4}$ + $FE_{C_2H_5OH}$) generally increases over the same range of current densities. Notably, **2** exhibits higher faradaic efficiency for H_2 than **3-Na** and **3-NaphOPO$_3$**. At a current density of −200 mA cm^{-2}, **3-Na** demonstrates the highest faradaic efficiency for C_1 products (FE_{CO} ∼ 30% + FE_{HCOOH} ∼ 30%) and the lowest faradaic efficiency for H_2 (∼17%). Under current densities ranging from −50 to −500 mA cm^{-2}, **3-NaphOPO$_3$** displays higher FE_{C2} products than the two other clusters, reaching up to ∼45% at −500 mA cm^{-2}, with respective faradaic efficiencies for C_2H_4 and C_2H_5OH of ∼30% and ∼15%. Compared with the VO_4 template, the internal PO_4 template and external naphthyl groups can promote C–C coupling, resulting in an increase in C_2 products. This observation indicates that CO_2RR properties are not solely reliant on surface morphology but also influenced by the internal VO_4/PO_4 tetrahedral template.

Moreover, we selected **3-Na** and **3-NaphOPO$_3$** clusters with a higher FE_{C1} as examples to evaluate their stability using chronoamperometric measurements. The current densities of gaseous products remained stable for at least 720 minutes, as shown in Fig. 7d and S29.† Despite minor fluctuations in the faradaic efficiencies of CO, C_2H_4, and H_2 at the start of the measurement, the overall current density remained relatively constant over the 720-minute period, indicating favorable catalytic sustainability. Finally, we compared these three clusters with atomically precise metal clusters exhibiting CO_2RR properties previously reported. As summarized in ESI Table 4,† it is worth noting that the CO selectivity of these three clusters is lower than that of gold clusters,[45] However, **3-NaphOPO$_3$** exhibits better faradaic efficiency for C_2 products, and copper, with its lower price, presents a more competitive alternative to gold.

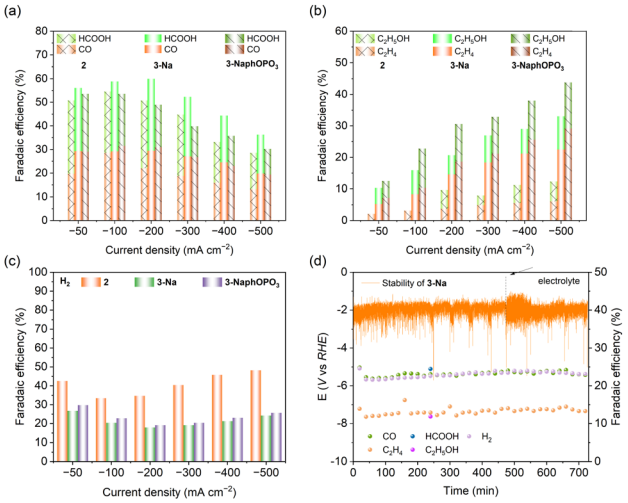

Fig. 7 Electrocatalytic performances. (a)–(c) Faradaic efficiencies of **2**, **3-Na**, and **3-NaphOPO$_3$** at different applied current densities (0.5 M $KHCO_3$). (d) Stability tests of the electrocatalysts for CO_2 reduction (**3-Na** at −200 mA cm^{-2}).

Conclusions

In conclusion, we present template-assisted strategies for the customization of seven high-nuclearity copper(I) alkynyl clusters at the atomic level. Single-crystal structural analysis reveals the multishelled core architecture of spherical Cu_{36} and Cu_{56} clusters assembled by a [M@(V/PO_4)$_6$] (M: Cu^{2+}, Na^+, K^+) skeleton, while the peanut-shaped Cu_{56} cluster is constructed using four separate PO_4 templates. The crystalline-state emissions of these clusters are dependent on the inner templates and outer phosphonate ligands. The enhanced luminescence observed can be attributed to numerous well-arranged intermolecular C–H···π interactions between the ligands of phenyl and 1-naphthyl phosphate protected clusters. The electrocatalytic properties of CO_2 reduction reaction are affected by both the surface morphology and the internal VO_4/PO_4 template. Specifically, internal PO_4 templates and external naphthyl groups could promote an increase in C_2 products. This study provides ingenious strategies for tailoring the structures of nanoclusters at an atomically precise level and highlights the significance of atomic-level comparative studies of structure–property relationships.

Data availability

All experimental and computational data are included in the ESI.† Crystallographic data for the structures reported in this

article have been deposited at the Cambridge Crystallographic Data Centre under deposition numbers CCDC 2219441, 2219447, 2116536, 2219449, 2219459, 2219463, 2219464, and 2285409.†

Author contributions

Y.-P. X. and X. L. conceived the original idea. Y.-P. X. designed and directed the synthesis experiments. J.-J. F. performed the experiments and analyzed the data. J.-J. F., Z. L., and Y.-L. S. performed the structural characterization. J.-J. F. collected and analyzed the ESI-MS, PL, and CO_2RR data. Y.-P. X. directed the DFT calculations. J.-J. F. conducted the DFT calculations. All authors have given approval to the manuscript.

Conflicts of interest

There are no conflicts to declare.

Acknowledgements

We gratefully acknowledge financial support from the National Natural Science Foundation of China (No. 21771071, 22171094, 21925104, and 92261204) and the Hubei Provincial Natural Science Foundation of China (No. 2021CFA020). We thank the staff in the Analytical and Testing Center at the Huazhong University of Science and Technology for all related measurements. We thank the staff at the BL17B beamline of the National Center for Protein Sciences Shanghai (NCPSS) at Shanghai Synchrotron Radiation Facility for the assistance with data collection.

References

1 R. Hamze, J. L. Peltier, D. Sylvinson, M. Jung, J. Cardenas, R. Haiges, M. Soleilhavoup, R. Jazzar, P. I. Djurovich, G. Bertrand and M. E. Thompson, *Science*, 2019, **363**, 601–606.
2 M. Cao, R. Pang, Q. Wang, Z. Han, Z. Wang, X. Dong, S. Li, S. Zang and T. C. W. Mak, *J. Am. Chem. Soc.*, 2019, **141**, 14505–14509.
3 S. Li, X. Du, B. Li, J. Wang, G. Li, G. Gao and S. Zang, *J. Am. Chem. Soc.*, 2018, **140**, 594–597.
4 R. Huang, Y. Wei, X. Dong, X. Wu, C. Du, S. Zang and T. C. W. Mak, *Nat. Chem.*, 2017, **9**, 689–697.
5 O. Fuhr, S. Dehnen and D. Fenske, *Chem. Soc. Rev.*, 2013, **42**, 1871–1906.
6 H. Schmidbaur and A. Schier, *Chem. Soc. Rev.*, 2012, **41**, 370–412.
7 Y. Sun, E. Wang, Y. Ren, K. Xiao, X. Liu, D. Yang, Y. Gao, W. Ding and Y. Zhu, *Adv. Funct. Mater.*, 2019, **29**, 1904242.
8 Z. Wang, M. Wang, Y. Li, P. Luo, T. Jia, R. Huang, S. Zang and T. C. W. Mak, *J. Am. Chem. Soc.*, 2018, **140**, 1069–1076.
9 P. Yuan, R. Chen, X. Zhang, F. Chen, J. Yan, C. Sun, D. Ou, J. Peng, S. Lin, Z. Tang, B. K. Teo, L. S. Zheng and N. Zheng, *Angew. Chem., Int. Ed.*, 2019, **58**, 835–839.
10 R. W. Huang, X. Y. Dong, B. J. Yan, X. S. Du, D. H. Wei, S. Q. Zang and T. C. W. Mak, *Angew. Chem., Int. Ed.*, 2018, **57**, 8560–8566.
11 L. L. Zhang and T. C. W. Mak, *Angew. Chem., Int. Ed.*, 2017, **56**, 16228–16232.
12 X. Chang, K. Low, J. Wang, J. Huang and C. Che, *Angew. Chem., Int. Ed.*, 2016, **55**, 10312–10316.
13 S. S. Y. Chui, M. F. Y. Ng and C. Che, *Chem.–Eur. J.*, 2005, **11**, 1739–1749.
14 R. P. Brocha Silalahi, G. Huang, J. Liao, T. Chiu, K. K. Chakrahari, X. Wang, J. Cartron, S. Kahlal, J. Saillard and C. W. Liu, *Inorg. Chem.*, 2020, **59**, 2536–2547.
15 Y. Jin, S. Li, Z. Han, B. J. Yan, H. Y. Li, X. Y. Dong and S. Q. Zang, *Angew. Chem., Int. Ed.*, 2019, **58**, 12143–12148.
16 K. K. Chakrahari, R. P. B. Silalahi, T. H. Chiu, X. Wang, N. Azrou, S. Kahlal, Y. C. Liu, M. H. Chiang, J. Y. Saillard and C. W. Liu, *Angew. Chem., Int. Ed.*, 2019, **58**, 4943–4947.
17 T. C. Higgs, P. J. Bailey, S. Parsons and P. A. Tasker, *Angew. Chem., Int. Ed.*, 2002, **41**, 3038–3041.
18 P. Putaj and F. Lefebvre, *Coord. Chem. Rev.*, 2011, **255**, 1642–1685.
19 H. Lv, Y. V. Geletii, C. Zhao, J. W. Vickers, G. Zhu, Z. Luo, J. Song, T. Lian, D. G. Musaev and C. L. Hill, *Chem. Soc. Rev.*, 2012, **41**, 7572–7589.
20 J. Zhang, Y. Huang, G. Li and Y. Wei, *Coord. Chem. Rev.*, 2019, **378**, 395–414.
21 J. Liu, L. Feng, H. Su, Z. Wang, Q. Zhao, X. Wang, C. Tung, D. Sun and L. Zheng, *J. Am. Chem. Soc.*, 2018, **140**, 1600–1603.
22 Z. Wang, H. Su, M. Kurmoo, C. Tung, D. Sun and L. Zheng, *Nat. Commun.*, 2018, **9**, 2094.
23 Y. Xie, J. Jin, X. Lu and T. C. W. Mak, *Angew. Chem., Int. Ed.*, 2015, **54**, 15176–15180.
24 Y. Xie and T. C. W. Mak, *J. Am. Chem. Soc.*, 2011, **133**, 3760–3763.
25 G. Gao, P. Cheng and T. C. W. Mak, *J. Am. Chem. Soc.*, 2009, **131**, 18257–18259.
26 L. Chen, F. Jiang, Z. Lin, Y. Zhou, C. Yue and M. Hong, *J. Am. Chem. Soc.*, 2005, **127**, 8588–8589.
27 S. Wang and G. Yang, *Chem. Rev.*, 2015, **115**, 4893–4962.
28 F. A. Paz, J. Klinowski, S. M. Vilela, J. P. Tome, J. A. Cavaleiro and J. Rocha, *Chem. Soc. Rev.*, 2012, **41**, 1088–1110.
29 K. J. Gagnon, H. P. Perry and A. Clearfield, *Chem. Rev.*, 2012, **112**, 1034–1054.
30 J. Goura and V. Chandrasekhar, *Chem. Rev.*, 2015, **115**, 6854–6965.
31 L. Zhang, R. Clérac, P. Heijboer and W. Schmitt, *Angew. Chem., Int. Ed.*, 2012, **51**, 3007–3011.
32 M. Haga, K. Kobayashi and K. Terada, *Coord. Chem. Rev.*, 2007, **251**, 2688–2701.
33 S. Bao and L. Zheng, *Coord. Chem. Rev.*, 2016, **319**, 63–85.
34 X. W. Lv, C. C. Weng, Y. P. Zhu and Z. Y. Yuan, *Small*, 2021, **17**, 2005304.
35 Y. Shen, J. Jin, J. Fang, Z. Liu, J. Shi, Y. Xie and X. Lu, *Inorg. Chem.*, 2021, **60**, 6276–6282.
36 J. Jin, Y. Xie, H. Cui, G. Duan, X. Lu and T. C. W. Mak, *Inorg. Chem.*, 2017, **56**, 10412–10417.

37 Y. Xie and T. C. W. Mak, *Angew. Chem., Int. Ed.*, 2012, **51**, 8783–8786.
38 L. Zhang and T. C. W. Mak, *J. Am. Chem. Soc.*, 2016, **138**, 2909–2912.
39 L. L. Zhang, G. Zhou, G. Zhou, H. Lee, N. Zhao, O. V. Prezhdo and T. C. W. Mak, *Chem. Sci.*, 2019, **10**, 10122–10128.
40 J. Fang, Y. Shen, Z. Liu, C. Liu, Y. Xie and X. Lu, *Inorg. Chem.*, 2021, **60**, 13493–13499.
41 V. W. W. Yam and K. K. W. Lo, *Chem. Soc. Rev.*, 1999, **28**, 323–334.
42 Z. N. Chen, N. Zhao, Y. Fan and J. Na, *Coord. Chem. Rev.*, 2009, **253**, 1–20.
43 H. Xu, D. Rebollar, H. He, L. Chong, Y. Liu, C. Liu, C. J. Sun, T. Li, J. V. Muntean, R. E. Winans, D. J. Liu and T. Xu, *Nat. Energy*, 2020, **5**, 623–632.
44 S. Nitopi, E. Bertheussen, S. B. Scott, X. Liu, A. K. Engstfeld, S. Horch, B. Seger, I. Stephens, K. Chan, C. Hahn, J. K. Norskov, T. F. Jaramillo and I. Chorkendorff, *Chem. Rev.*, 2019, **119**, 7610–7672.
45 D. Raciti and C. Wang, *ACS Energy Lett.*, 2018, **3**, 1545–1556.
46 Y. Song, Y. Li, M. Zhou, X. Liu, H. Li, H. Wang, Y. Shen, M. Zhu and R. Jin, *Sci. Adv.*, 2021, **7**, eabd2091.
47 X. Ma, J. Jia, P. Luo, Z. Wang, S. Zang and T. C. W. Mak, *Nano Res.*, 2022, **15**, 5569–5574.
48 S. Nematulloev, R. W. Huang, J. Yin, A. Shkurenko, C. Dong, A. Ghosh, B. Alamer, R. Naphade, M. N. Hedhili, P. Maity, M. Eddaoudi, O. F. Mohammed and O. M. Bakr, *Small*, 2021, **17**, 2006839.
49 J. Wang, F. Xu, Z. Y. Wang, S. Q. Zang and T. C. W. Mak, *Angew. Chem., Int. Ed.*, 2022, **61**, e202207492.
50 Z. J. Guan, J. J. Li, F. Hu and Q. M. Wang, *Angew. Chem., Int. Ed.*, 2022, **61**, e202209725.
51 H. Seong, V. Efremov, G. Park, H. Kim, J. S. Yoo and D. Lee, *Angew. Chem., Int. Ed.*, 2021, **133**, 14684–14691.
52 S. Verma, Y. Hamasaki, C. Kim, W. Huang, S. Lu, H. M. Jhong, A. A. Gewirth, T. Fujigaya, N. Nakashima and P. J. A. Kenis, *ACS Energy Lett.*, 2018, **3**, 193–198.
53 X. Wan, J. Wang, Z. Nan and Q. Wang, *Sci. Adv.*, 2017, **3**, e1701823.
54 Q. Tang, Y. Lee, D. Li, W. Choi, C. W. Liu, D. Lee and D. Jiang, *J. Am. Chem. Soc.*, 2017, **139**, 9728–9736.
55 L. J. Liu, Z. Y. Wang, Z. Y. Wang, R. Wang, S. Q. Zang and T. C. W. Mak, *Angew. Chem., Int. Ed.*, 2022, **61**, e202205626.
56 X. Ma, F. Sun, L. Qin, Y. Liu, X. Kang, L. Wang, D. Jiang, Q. Tang and Z. Tang, *Chem. Sci.*, 2022, **13**, 10149–10158.
57 P. Yang and U. Kortz, *Acc. Chem. Res.*, 2018, **51**, 1599–1608.
58 S. Peng, H. Yang, D. Luo, M. Xie, W. Tang, G. Ning and D. Li, *Inorg. Chem. Front.*, 2022, **9**, 5327–5334.
59 Y. Xie, Y. Shen, G. Duan, J. Han, L. Zhang and X. Lu, *Mater. Chem. Front.*, 2020, **4**, 2205–2222.
60 T. Lu and F. Chen, *J. Comput. Chem.*, 2012, **33**, 580–592.
61 F. Neese, F. Wennmohs, U. Becker and C. Riplinger, *J. Chem. Phys.*, 2020, **152**, 224108.
62 G. F. Manbeck, W. W. Brennessel, R. A. Stockland and R. Eisenberg, *J. Am. Chem. Soc.*, 2010, **132**, 12307–12318.